



Effect of ultrasonic processing duration on the microstructure evolution and applied performance of ternary Cu-Sn-Bi immiscible alloy

Ying Zhang¹ · Wenhua Wu¹ · Jianyuan Wang¹ · Wei Zhai¹

Received: 15 July 2025 / Accepted: 16 September 2025 / Published online: 25 September 2025
© The Author(s), under exclusive licence to Springer-Verlag GmbH Germany, part of Springer Nature 2025

Abstract

Three-dimensional (3D) orthogonal ultrasounds were introduced into ternary Cu-33%Sn-15%Bi immiscible alloy to control its liquid-phase separation. Compared to the layered structure formed under static condition, homogeneous dispersion of Bi-rich particles within the Cu₃Sn matrix was facilitated by employing short-time ultrasounds during the final stage of liquid-phase separation. Conversely, long-time ultrasounds application throughout liquid-phase separation generated limited macro-segregation suppression effect. Numerical simulations indicated that although long-time ultrasounds enhanced droplet nucleation, it also induced significant acoustic shielding from cavitation bubbles, causing severe attenuation of acoustic energy and consequent reduction in droplet fragmentation and migration. This phenomenon weakened the fragmentation and the migration of Bi droplets. The homogeneous and refined microstructure produced by short-time 3D ultrasounds possessed superior electrochemical corrosion and wear-resisting properties. This work demonstrates that employing an appropriate ultrasonic processing time can inhibit cavitation-induced acoustic shielding and maximize energy utilization efficiency.

Keywords Three-dimensional ultrasounds · Immiscible alloy · Liquid-phase separation · Ultrasounds duration · Secondary droplet

1 Introduction

Immiscible alloys have emerged as critical structural materials in advanced engineering applications ranging from tribological components to thermal management systems, owing to their unique ability to combine disparate properties through controlled phase architectures [1–3]. The archetypal challenge in fabricating these alloys lies in mitigating the inherent segregation resulting from the migration and coalescence of secondary droplets driven by Marangoni and Stokes effects [4–6]. Such segregation phenomena not only degrade mechanical properties but also compromise functional performance through discontinuous electrical/thermal transport pathways [7–10].

✉ Wei Zhai
zhaiwei322@nwpu.edu.cn

¹ MOE Key Laboratory of Materials Physics and Chemistry under Extraordinary Conditions, Northwestern Polytechnical University, Xi'an 710072, P. R. China

Recent studies have shown that the application of high-intensity power ultrasound in liquid immiscible alloys is beneficial to the formation of uniformly dispersed monotectic microstructure [11–13]. For example, Kotadia et al. [12] found that introducing ultrasound into the liquid Al-Sn-Cu immiscible alloy allowed the soft Sn particles to be uniformly distributed within the hard Al-rich matrix. Komarov et al. [9] demonstrated that the periodic expansion and collapse of cavitation bubbles in the melt is the primary factor in refining Bi-rich droplets. In addition, our research group proved that the high pressure in the cavitation region significantly accelerates the uniform nucleation of secondary (Bi) droplets by modelling the liquid phase separation of immiscible alloys within ultrasonic field [13]. This principle of microstructural control through external energy fields finds parallels in studies of Pt₃Al and RuAl systems, where strategic interventions like transition metal doping are employed to tailor mechanical and surface properties [14, 15]. Although these studies underscore the utility of ultrasound in immiscible alloys, the temporal aspects of

ultrasonic processing remain poorly understood. It is known that continuous ultrasound application enhances droplet nucleation and restricts Stokes migration [16, 17]. However, extended ultrasound application leads to gas nucleation and bubble growth [18, 19], which cause acoustic shielding and attenuate ultrasonic efficiency [20]. These opposing effects underline the critical importance of ultrasonic processing duration, yet a systematic investigation into how ultrasounds duration influences phase separation mechanisms is still lacking. Furthermore, although statistical tools such as analysis of variance (ANOVA) have been employed to quantify the influence of parameters like frequency and amplitude on mechanical properties [21, 22] or machining outcomes [23], a comprehensive framework correlating ultrasonic processing duration with microstructural evolution and performance remains absent. Thus, there is an urgent need to unravel the liquid-phase separation mechanisms under varying ultrasounds duration and to develop predictive insights that can guide process optimization. This study aims to address this gap through an integrated approach combining multiphysics modeling and experimental validation.

In this paper, ternary Cu-33%Sn-15%Bi immiscible alloy was used to investigate the time-dependence of ultrasonic vibration on microstructural evolution and applied performance through two distinct ultrasonic conditions: long-time irradiation ($t=20$ s) throughout liquid-phase separation process and short-time irradiation ($t=5$ s) during the final stage of liquid-phase separation. To quantitatively evaluate the ultrasonic impact, we employed a multiphysical model coupled with nonlinear acoustic pressure and acoustic streaming simulations to quantify key influence metrics, including the spatial distribution of sound pressure, the volume fraction of the cavitation zone, the intensity of acoustic streaming, and the nucleation rate and size distribution of secondary droplets. On this basis, the relationship between the ultrasound application and the electrochemical and wear-resisting properties was further investigated.

2 Experimental procedure and simulation model

2.1 Experimental procedure

High-purity Cu (99.99 wt%), Sn (99.99 wt%) and Bi (99.99 wt%) were used as raw materials to prepare a 151.5 g Cu-33%Sn-15%Bi immiscible alloy. These experiments were performed using a 3D ultrasonic solidification apparatus, and its schematic diagram was displayed in previous work [24]. In the experiment, Cu and Sn elements were first placed into a graphite crucible, melted and heated to approximately 1560 K using high-frequency induction melting and

subsequently held preservation for 5 min. Then, Bi element was added to the molten alloy, and the high-frequency current was adjusted to maintain the melt temperature at about 1280 K for 2 min for the formation of a homogeneous liquid. After that, the molten alloy was poured into a preheated square graphite mold with internal dimensions of $20 \times 20 \times 49$ mm, a thickness of 6.5 mm, and a preheating temperature of ~ 900 K. Three SONIC VCX1500 ultrasonic transducers with an operating frequency of 20 kHz and an amplitude of 22 μm were set up at the center point of the bottom and side-walls of the mold. Meanwhile, an XSR90-04V0 paperless recorder, coupled with a 2 mm-diameter K-type NiCr-NiSi thermocouple, was used to measure the cooling curve at the center of the sample. To investigate the time-dependence of ultrasonic vibration on the microstructural morphology and subsequent applied performance of the sample, two kinds of ultrasonic conditions were employed: (1) three ultrasonic transducers were simultaneously activated at the temperature stage of 1011–983 K (final of the liquid-phase separation); (2) three ultrasonic transducers were simultaneously activated at the temperature stage of 1067–983 K (beginning of the liquid-phase separation). The above experimental cases are defined as short-time ultrasounds ($t_{US}=5$ s) and long-time ultrasounds ($t_{US}=20$ s), respectively. It is noteworthy that the actual duration of ultrasonic processing depends on the cooling rate of the melt. The values of 20 s and 5 s reported here are specific to the experimental conditions employed in this study. To ensure reproducibility and result uniqueness, all solidification experiments followed a strict protocol. The cooling curves and liquid-phase separation interval (1067–983 K) remained stable across all replicates. Ultrasonic parameters were precisely calibrated and monitored before each experiment to ensure consistent power input.

After the experiment, the alloy samples were cut longitudinally and polished, and the corresponding thermal analysis was conducted by a Netzsch STA 449 C simultaneous thermal analyzer with a scanning rate of 10 K/min. The phase composition and solidification microstructure were characterized by an X-ray diffractometer (XRD, D8 Discover A25), a scanning electron microscope (SEM, FEI Sirion 200), and an energy-dispersive spectrometer (EDS, INCA Energy 300). Finally, the electrochemical corrosion resistance was evaluated at room temperature by a CHI600E electrochemical workstation with 3.5% NaCl aqueous solution as the electrolyte. Liquid metal friction and wear testing machine (LMT-100) and CGr15 grinding ball with a diameter of 6.00 mm were used to determine the wear-resisting properties of the alloy samples. These samples were tested by dry sliding rubbing at room temperature with a positive load of 10 N, and the sliding distance was 1 mm, operated at a frequency of 3 Hz for 20 min.

2.2 Simulation model

A 3D finite element model was established to simulate the acoustic field and flow field distribution within Cu-33%Sn-15%Bi liquid alloy, as shown in Fig. 1 (a). The spatial characteristics of the acoustic and flow fields within YZ section of the sample are subsequently analyzed. The calculation process of this multiphysics model is given in Fig. 1 (b). In the simulation, the vibration characteristic of the mold excited by a 3D ultrasonic source is calculated by the following formula [25]:

$$-\rho_m \omega^2 \mathbf{u} = \nabla \cdot \mathbf{S} \quad (1)$$

where ρ_m represents the density of the graphite mold, ω is the angular frequency, \mathbf{u} denotes the displacement vector and \mathbf{S} is the stress tensor. The calculated displacement of the inner wall of the mold is used as the vibration source and input into the acoustic field model. The sound field within Cu-33%Sn-15%Bi liquid alloy can be calculated by a nonlinear inhomogeneous Helmholtz equation:

$$\nabla^2 P + k_c^2 P = 0 \quad (2)$$

in which P represents the acoustic pressure and k_c is the acoustic wave vector. Considering the energy loss caused by the cavitation effect, the square of k_c satisfies the following relationship:

$$\Re(k_c^2) = \frac{\omega^2}{c^2} + \frac{4\pi R_0 N_b \omega^2}{\omega_0^2 - \omega^2} \quad (3)$$

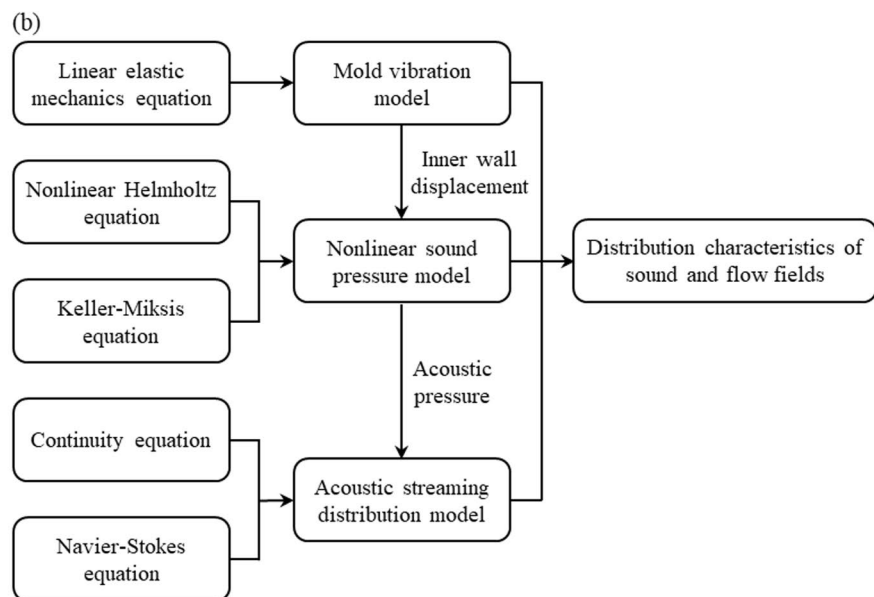
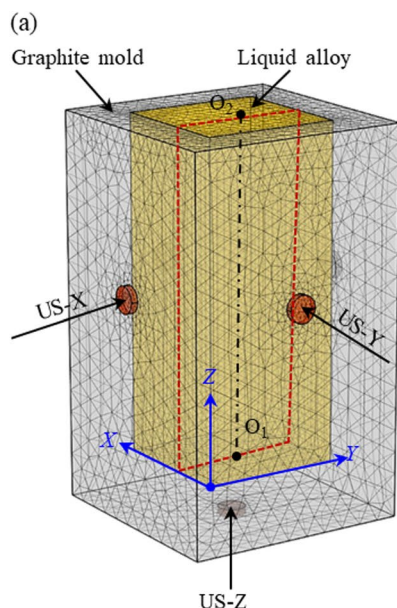


Fig. 1 Schematic diagram of modelling the 3D sound and flow fields within Cu-33%Sn-15%Bi liquid alloy. (a) 3D geometric model; (b) flow chart

where ω_0 and R_0 represent the resonant frequency and the initial radius of the bubble, respectively. N_b denotes the

$$\Im(k_c^2) = -2\rho\omega N_b \frac{\Pi_{th} + \Pi_v + \Pi_r}{|P|^2} \quad (4)$$

bubble number density in the liquid. ρ and c are the liquid density and sound speed, respectively. Π_{th} , Π_v and Π_r stand for heat dissipation, viscous dissipation and acoustic radiation force dissipation, respectively. Additionally, the acoustic attenuation coefficient α is strongly correlated with the acoustic pressure amplitude and bubble oscillations.

The radial dynamics of cavitation bubbles can be described by the classical Keller-Miksis equation [26]:

$$\rho \left(\left(1 - \frac{1}{c} \frac{dR}{dt} \right) R \frac{d^2 R}{dt^2} + \frac{3}{2} \left(\frac{dR}{dt} \right)^2 \left(1 - \frac{1}{3c} \frac{dR}{dt} \right) \right) = \left(1 + \frac{1}{c} \frac{dR}{dt} + \frac{R}{c} \frac{d}{dt} \right) \left(P_g + P_v - \frac{2\sigma}{R} - \frac{4\mu}{R} \frac{dR}{dt} - P_0 + P_A \right) \quad (5)$$

in which μ is the viscosity, σ is the surface tension between bubble and liquid melt. R denotes the instantaneous bubble radius. P_0 and P_v represent the static pressure and the saturated vapor pressure inside the bubble, respectively. $P_A = P_a \sin(2\pi f t)$, where P_a is the driving acoustic pressure and f is the ultrasonic frequency. The above results are then incorporated into the continuity Eq. (6) and the Navier-Stokes Eq. (7) to further calculate the spatial distribution characteristics of the flow field in the liquid alloy under 3D ultrasonic conditions [27, 28]:

$$\nabla \cdot \mathbf{U} = 0 \quad (6)$$

$$-\nabla \cdot (-P\mathbf{I} - \boldsymbol{\tau}) + \rho (\mathbf{U} \cdot \nabla) \mathbf{U} = \mathbf{F} \quad (7)$$

where \mathbf{U} , \mathbf{I} and $\boldsymbol{\tau}$ represent the flow velocity, unit matrix, and pressure tensor of viscosity, respectively. \mathbf{F} denotes the acoustic radiation force per unit volume, which can be calculated by the spatial variation of the Reynolds stress [27]:

$$\mathbf{F}_j = -\frac{\partial(\rho u_i u_j)}{\partial x_i} \quad (8)$$

in which the overline denotes the time-averaged value over one oscillation period, and u represents the vibration velocity. The acoustic radiation force is calculated by substituting the acoustic pressure into Eq. (8), and the flow distribution within the molten alloy is then simulated by solving Eqs. (6) and (7). The entire computational domain is divided into 128,717 mesh elements. The physical parameters used in the model are listed in Table 1.

3 Results and discussion

3.1 Thermal analysis and phase constitution

The phase transformation process of the alloy under near-equilibrium solidification conditions was analyzed by DSC, as shown in Fig. 2(a). According to the DSC curves, six endothermic and six exothermic peaks are observed during the heating and cooling periods, respectively. Based on

the published Cu-Sn-Bi phase diagram [30, 31], the phase transformation sequence during cooling is as follows: the first small exothermic peak deviation from the baseline at 1067 K is due to the phase separation of liquid Cu₃Sn-rich and Bi-rich phases L → L₁ (Cu₃Sn-rich) + L₂ (Bi-rich). Subsequently, two pronounced exothermic peaks emerge at 982 K and 872 K, denoting the monotectic transformation L₁ → γCu₃Sn + L₂ and the solid phase transition γ → εCu₃Sn. Then, the eutectic transformation L₂ → (Sn) + ηCu₆Sn₅ and peritectic reaction L₂ + εCu₃Sn → (Bi) + ηCu₆Sn₅ take place when the temperature drops to 497 K and 440 K, respectively. Finally, a weak exothermic peak observed at 403 K corresponds to the eutectic reaction L₂ → (Sn) + (Bi). Hence, it can be concluded that the final solidification microstructure of the sample should be composed of Cu₃Sn, (Bi), Cu₆Sn₅, and (Sn) phases, which is confirmed by the XRD diffraction analysis results, as shown in Fig. 2(b).

Cu₃Sn and (Bi) are the two primary phases in the alloy samples under different solidification conditions. Besides, minor Cu₆Sn₅ intermetallic compound and (Sn) solid solution phase are also observed. The cooling curves are shown in Fig. 2(c), where the solidification stages of ultrasonic action are marked by the blue line segment. It can be observed that the temperature at the end of liquid phase separation remains consistent at 983 K under both static and ultrasonic conditions. Long-time ultrasounds ($t_{US}=20$ s) are applied throughout the liquid phase separation process (1067–983 K), whereas short-time ultrasounds ($t_{US}=5$ s) are applied only during the final stage of the liquid phase separation process (1011–983 K).

3.2 Morphological characteristics of solidified structures

Figure 3 shows the macroscopic structural patterns of ternary Cu-33%Sn-15%Bi alloy samples solidified under different solidification conditions. Under static solidification (Fig. 3(a)), pronounced macrosegregation along the vertical direction is observed: Bi-rich phase accumulates at the sample bottom, accounting for approximately 11% of the total volume, while Cu₃Sn phase predominantly occupies the middle and upper regions. A distinct boundary marked by the blue dashed line separates Bi-rich and Cu₃Sn zones. As observed in Fig. 3(b), short-time ultrasounds completely eliminate Bi-rich segregation layer. Nevertheless, the area proportion of Bi-rich segregation layer has increased to 3.9% as the ultrasound action time extends to 20 s, as shown in Fig. 3(c). Additionally, noticeable pores are observed on the surface of samples treated by ultrasound. The gas phase volume fraction in the alloy sample, defined as $V=V_g/V_a \times 100\%$ (where V_a and V_g denote the total sample volume and the gas phase volume, respectively), is quantified with different

Table 1 Physical parameters used for calculation

Parameter	Value	Unit
Graphite mold density ρ_m	1.82×10^3	kg/m ³
L ₁ phase density ρ_1 [10]	7.75×10^3	kg/m ³
L ₂ phase density ρ_2 [10]	9.41×10^3	kg/m ³
Sound speed c in liquid melt [9]	3.09×10^3	m/s
L ₁ phase velocity μ_1 [10]	1.82×10^{-3}	Pa·s
L ₂ phase velocity μ_2 [10]	1.3×10^{-3}	Pa·s
Surface tension between bubble and liquid melt σ [29]	0.34	N/m
Static pressure P_0 [26]	1.01×10^5	Pa
Saturated vapor pressure inside bubble P_v [17]	2.34×10^3	Pa
Ultrasonic frequency f	20	kHz
Initial bubble radius R_0	5	μm
Gas conductivity k_g [26]	2.6×10^{-2}	W/(m·K)
Adiabatic exponent n_f [26]	1.4	/
Temperature inside bubble T_g [13]	2.73×10^2	K
Period of sound wave τ_0	50	μs
L ₂ phase interfacial tension γ [30]	6.4×10^{-1}	N/m
Nucleation constant J_0 [17]	1×10^{17}	1/(m ³ ·s)
Liquid-liquid interfacial free energy σ_{LL} [17]	2×10^{-2}	J/m ²
L ₁ phase molecular volume V_1 [13]	9.13×10^{-6}	m ³ /mol
L ₂ phase molecular volume V_2 [13]	2.2×10^{-5}	m ³ /mol
Latent heat of liquid phase separation ΔH [13]	1.08×10^4	J/mol

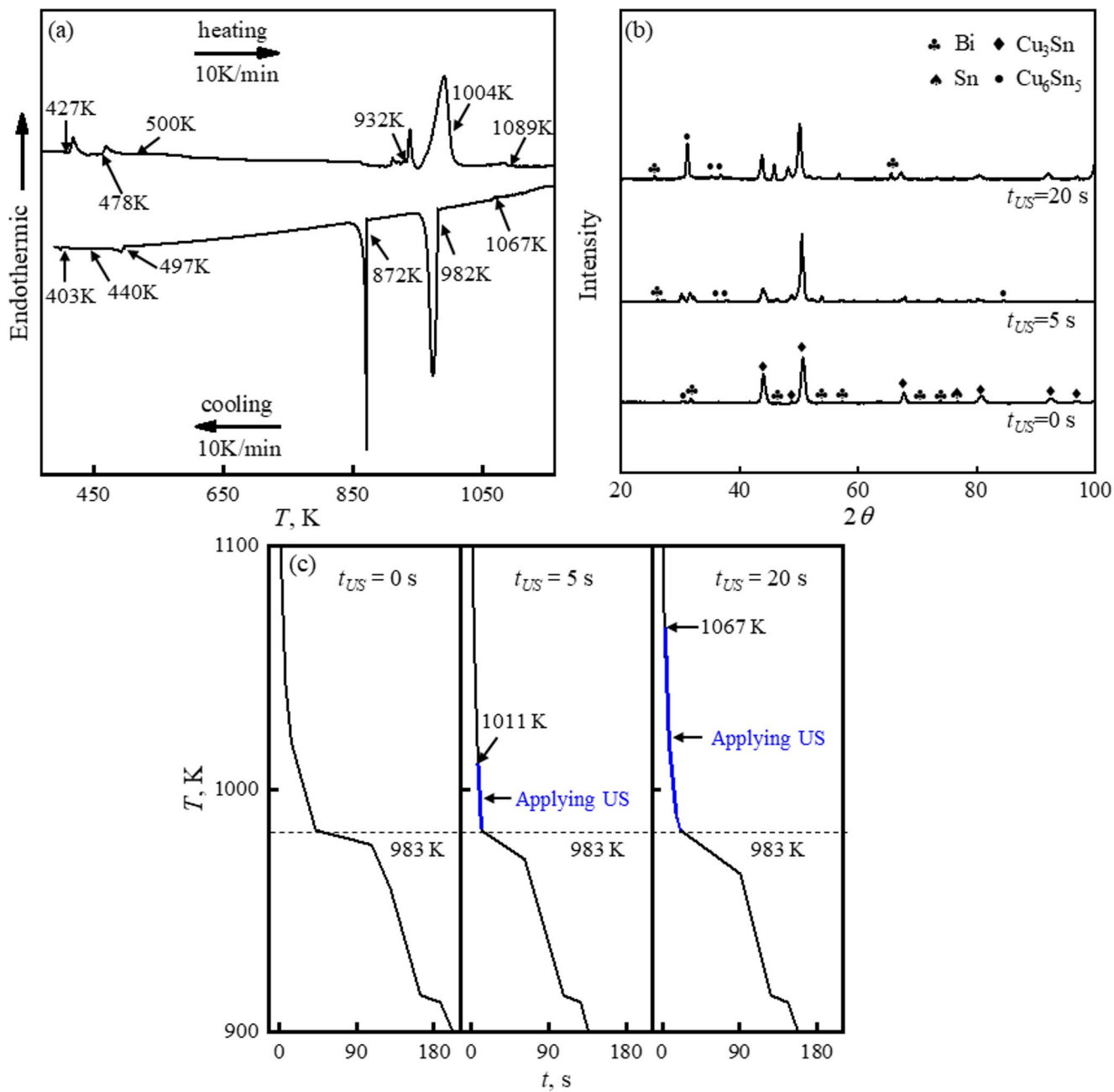


Fig. 2 Thermal analysis and phase constitution of ternary Cu-33%Sn-15%Bi alloy under different solidification conditions. **(a)** DSC curves; **(b)** XRD patterns; **(c)** cooling curves

solidification conditions in Fig. 3(d). The gas phase volume fraction under static solidification condition is measured as about 0.07%. Long-time ultrasounds significantly increase this value to 3.60%, which is 12.4 times higher than that of short-time ultrasounds. This marked enhancement is primarily originated from the ultrasonic-activated nucleation and subsequent growth of dissolved gases within the liquid metal [18, 19]. Moreover, the solid Cu₃Sn primary phase begins to nucleate when ultrasound is turned off at the end of liquid-phase separation (983 K), which is accompanied

by a significant increase in melt viscosity, thereby inducing entrapment of partial gas bubbles within Cu₃Sn matrix. Therefore, the gas volume fraction climbs up evidently with prolonged ultrasonic treatment duration.

Figure 4 shows the microstructure variation along the height direction of Cu-33%Sn-15%Bi immiscible alloy, where the black and white phases respectively correspond to Bi-rich and Cu₃Sn phase formed during the liquid-phase separation process, and the grey-banded phase represents (Bi) + (Sn) eutectic phase. Under static condition, many

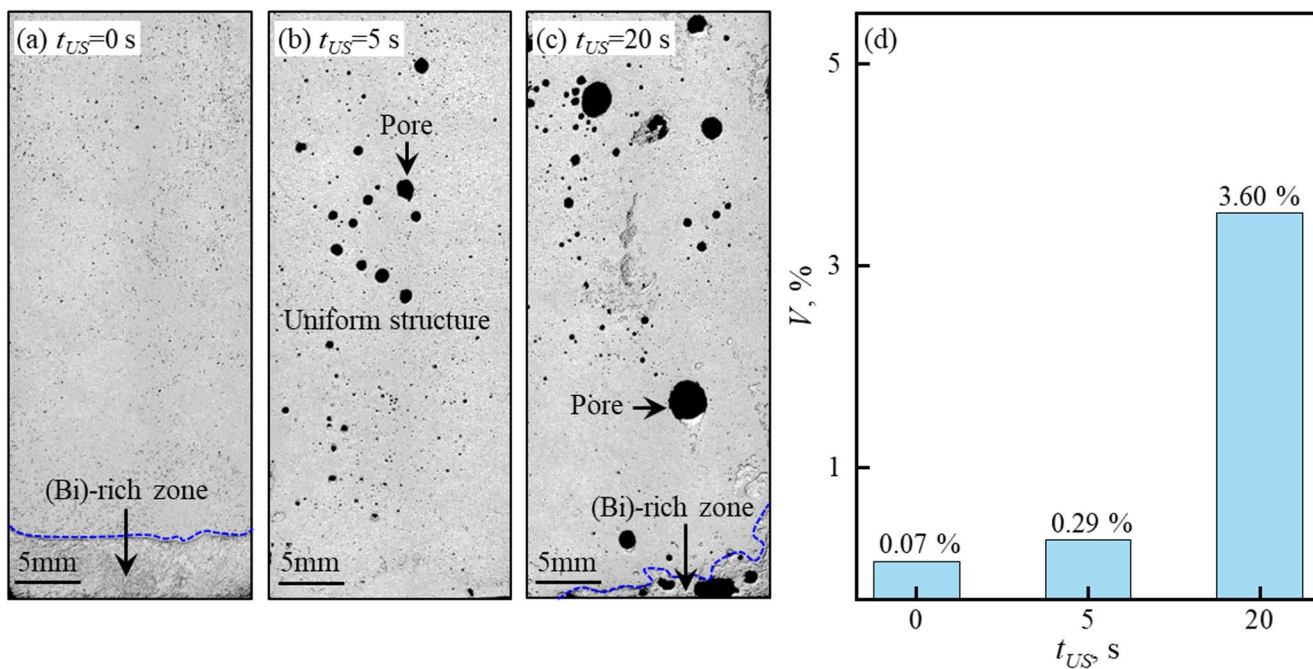


Fig. 3 Macroscopic structural characteristics of Cu-33%Sn-15%Bi alloy solidified with various ultrasonic processing time. (a) $t_{US}=0$ s; (b) $t_{US}=5$ s; (c) $t_{US}=20$ s; (d) gas volume fraction within alloy samples

nearly spherical Bi-rich particles are distributed within Cu_3Sn matrix across the top and middle regions of the sample. Conversely, the short clavate or spherical Cu_3Sn phases and (Bi) + (Sn) eutectic are dispersed at the bottom Bi-rich zone, as seen in Fig. 4(a). In Fig. 4(b), it can be seen that the irregular shape Bi-rich particles almost evenly distribute in the whole alloy sample to form a uniform structure under short-time ultrasonic condition ($t_{US}=5$ s). However, applying 20 s ultrasounds induces Cu_3Sn phases in the bottom region, as shown in Fig. 4(c). These Cu_3Sn phases are transformed from short clavate to cluster, while maintaining similar to the static at the top and middle regions, as shown in Fig. 4(c).

To explore the spatial distribution of macroscopic solute, the contents of Cu, Sn, and Bi elements within five regions from top to bottom of the alloy sample are quantitatively determined using EDS analysis technology. As demonstrated in Figs. 5(a) and (b), Cu and Sn elements maintain comparable levels throughout the regions 1–4 under both static and long-time ultrasounds conditions, while exhibiting a significant decrease in the region 5. Short-time ultrasounds condition induces solute redistribution, achieving near-uniform distribution of Cu and Sn elements across all spatial regions. Additionally, the distribution of Bi element shows axial homogeneity under short-time ultrasounds condition, whereas it remains basically consistent in regions 1–4 with marked accumulation in region 5 under static.

and long-time ultrasounds conditions. The above results indicate that short-time ultrasounds effectively suppress

element segregation. Moreover, the average size distribution of (Bi) particle under different solidification conditions is also analyzed and the result is given in Fig. 5(d). It can be observed that the average size of (Bi) particle remains.

relatively uniform throughout the melt under short-time ultrasounds condition, suggesting that short-time ultrasounds have dual efficacy in both eliminating solute element segregation and promoting uniform distribution of refined Bi-rich phases.

3.3 Effects of cavitation and acoustic streaming on liquid phase separation

3.3.1 Distribution of sound and flow field within liquid melt

As shown in Fig. 3, the gas content in the melt increases significantly after long-time ultrasonic treatment, which affects the distribution of the sound and flow fields. Utilizing the quantified gas phase volume fraction presented in Fig. 3(d), numerical simulations are conducted to reveal the stable distribution of sound and flow field within the melt under differential ultrasounds durations, as shown in Fig. 6. The sound pressure distributions under different ultrasound application time are presented in Fig. 6(a), in which the yellow lines represent the isolines of cavitation threshold calculated by the following equation [30]:

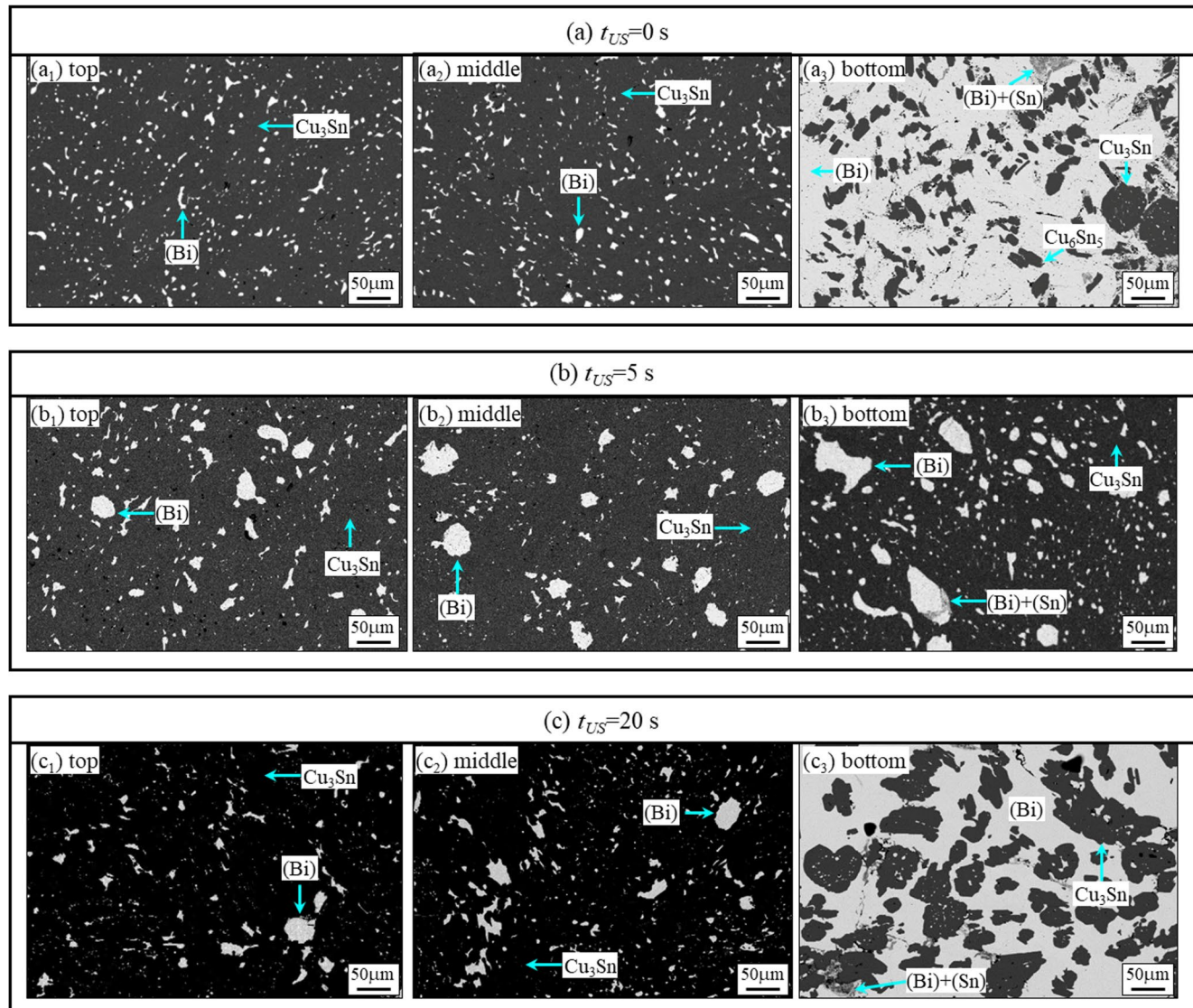


Fig. 4 Solidification microstructure at top, middle and bottom parts. (a) $t_{US}=0\text{ s}$; (b) $t_{US}=5\text{ s}$; (c) $t_{US}=20\text{ s}$

$$P_b = P_0 - P_v + \frac{2}{3\sqrt{3}} \left(\frac{2\sigma}{R_0} \right)^{\frac{3}{2}} \left(P_0 - P_v + \frac{2\sigma}{R_0} \right)^{-\frac{1}{2}} \quad (9)$$

The cavitation region is quantitatively defined as the region where localized pressure exceeds the Blake threshold ($P_b=0.21\text{ MPa}$). Comparative analysis reveals a striking inverse proportionality between the ultrasounds duration and the volume proportion of the cavitation region: the cavitation region almost covers the entire melt under short-time ultrasounds condition, whereas it occupies only 28% of the entire melt under long-time ultrasounds condition, as

demonstrated in Fig. 6(a). Figure 6(b) depicts the flow field distribution on the longitudinal section of the melt, where the grey arrow and its density indicate the flow direction and the magnitude, respectively. The acoustic streaming profiles

under both two ultrasound conditions are similar. Two jets induced by the sound pressure gradient are generated at the contact surfaces between the ultrasonic horn and the mold sidewall and bottom, which propagate radially until reaching the opposite wall and then spreading up and down, ultimately forming two near-spherical vortexes. Figures 6(c) and (d) give the sound pressure and flow velocity profiles along the symmetry axis O₁O₂ under different ultrasound application time. The sound pressure decreases along the symmetry axis O₁O₂, but its maximum value under short-time ultrasounds is 6.73 MPa, which is evidently higher than that of 2.06 MPa under long-time ultrasounds condition. The flow velocity increases from 0 cm/s to a maximum value of 28.6 cm/s at $z=3.5\text{ mm}$ as it propagates along the O₁O₂ axis under long-time ultrasounds condition, whereas its maximum value

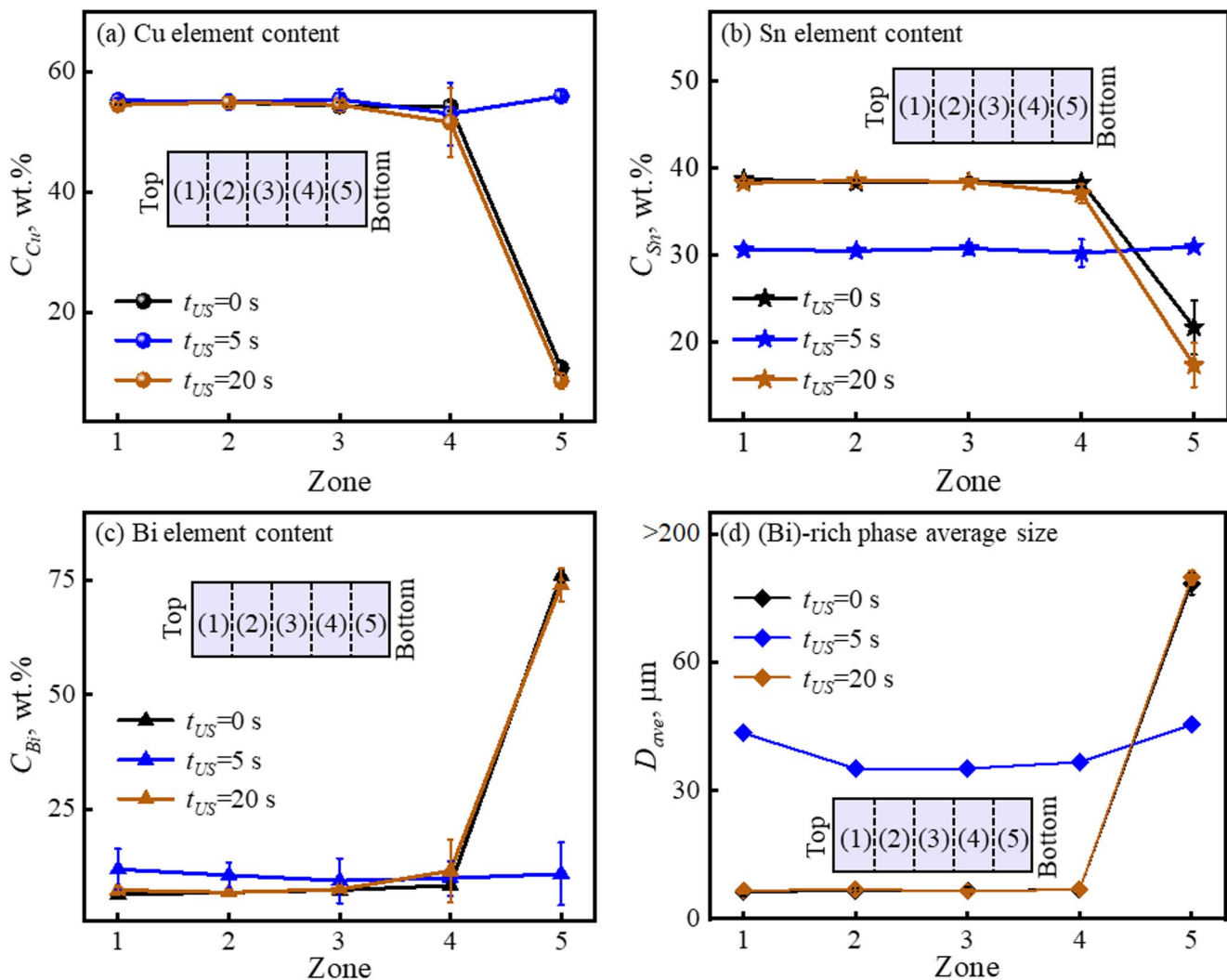


Fig. 5 Phase separation characteristics. (a)-(c) the solute distribution of Cu, Sn and Bi elements determined by EDS analysis technology; (d) the average size of (Bi) particles

under short-time ultrasounds condition is about 39.2 cm/s at \$z=28\$ mm. Notably, the distribution patterns of sound and flow fields within the liquid melt show no obvious change with increased ultrasound application time. However, the volume fraction of the cavitation region and the magnitudes of sound pressure and flow velocity are significantly reduced with the increase in ultrasounds duration. This phenomenon is primarily attributed to the increased bubble content under long-time ultrasounds condition, which intensifies the acoustic shielding effect caused by cavitation bubbles and consequently accelerates acoustic attenuation in the melt.

3.3.2 Nucleation and growth of Bi-rich phase droplets facilitated by ultrasonic cavitation

The liquid-phase separation mechanisms of Cu-33%Sn-15%Bi immiscible alloy within 3D ultrasonic field are

further investigated. The nucleation rate of Bi-rich droplets can be calculated using the following Eqs [5, 32, 33]. :

$$J = J_0 \times \exp \left(-\frac{\Delta G \times f(\theta)}{k_b \cdot T} \right) \quad (10)$$

where \$J_0\$ means the nucleation constant, \$f(\theta)=(1-\cos\theta)^2 \cdot (\cos\theta + 2)/4\$ is geometric factor, in which \$\theta\$ stands for the wetting angle, \$k_b\$ denotes Boltzmann constant, \$T\$ is the temperature of the melt. \$\Delta G\$ is the energy barrier for the formation of a critical nucleus, obtained by [32]:

$$\Delta G = \frac{16\pi}{3} \times \frac{\sigma_{LL}^3 T_l^2 V_2^2}{\Delta H^2 \Delta T^2} \quad (11)$$

in which \$\sigma_{LL}\$ is liquid-liquid phase interfacial free energy, \$T_l\$ is the liquidus temperature, \$V_2\$ means the molar volume and

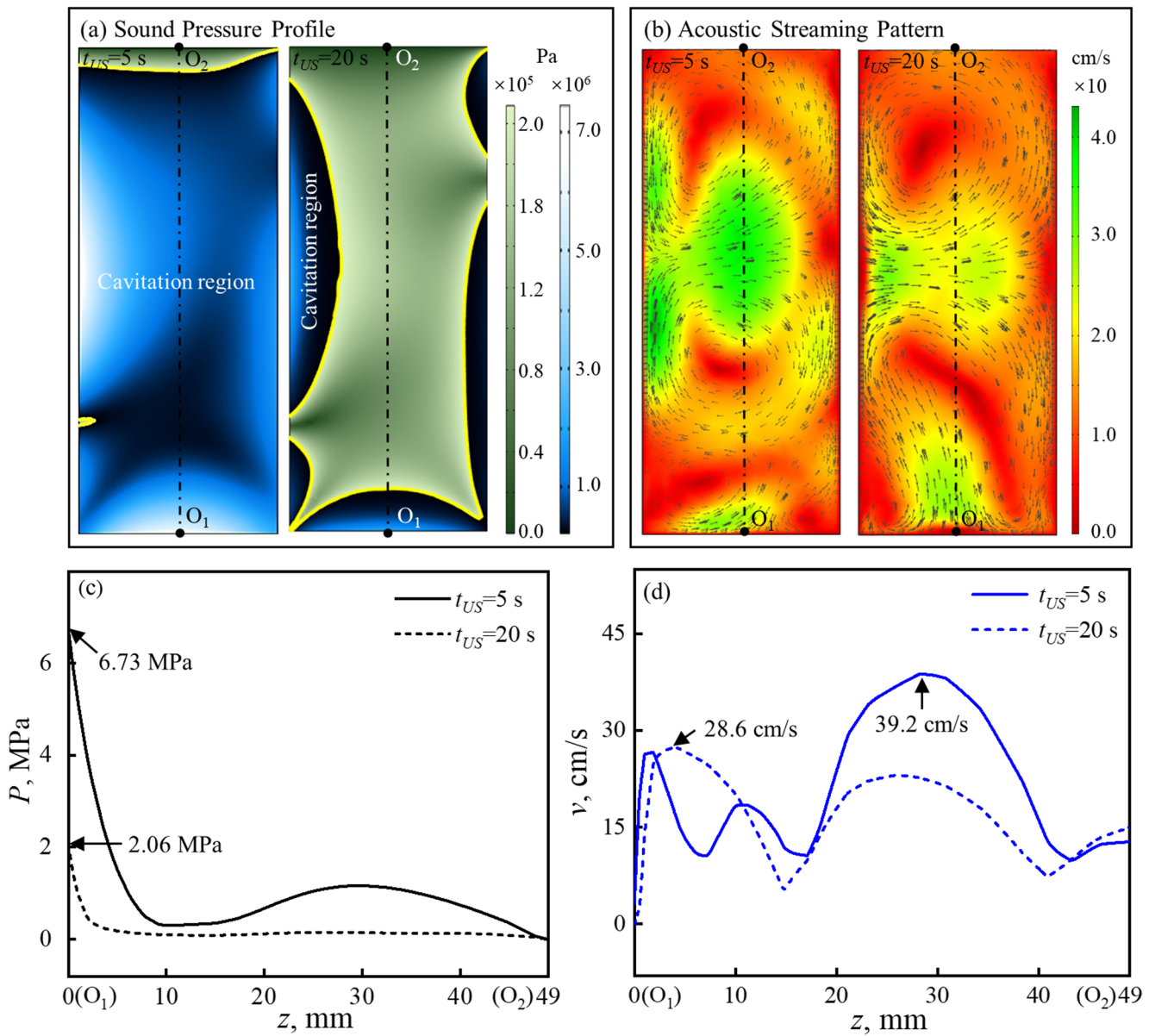


Fig. 6 Stable sound pressure and acoustic streaming along the longitudinal direction within liquid alloy. (a) sound pressure profile; (b) acoustic streaming pattern; (c) the variation of sound pressure along the symmetry axis O₁O₂; (d) flow velocity varies with the height of z-axis

ΔH is the heat of phase change. The undercooling ΔT can be calculated by the Clausius-Clapeyron equation [33]:

$$\Delta T = T_l - T_0 + \frac{T_l \Delta V}{\Delta H} \times (P - P_0) \quad (12)$$

where P is the instantaneous sound pressure. The number density of Bi-rich phase droplets in melt $n = J \times \Delta t$, in which Δt denotes the duration of heterogeneous nucleation induced by ultrasound. Therefore, the spatial distribution characteristics of Bi-rich phase droplets number density in the melt under different ultrasounds durations can be.

calculated by solving Eqs. (10)-(12) simultaneously, and the results are shown in Fig. 7(a). Short-time ultrasounds condition promote nucleation predominantly in regions except the melt top, and its maximum number density is about $5.0 \times 10^{28} \text{ m}^{-3}$. Conversely, long-time ultrasounds induce Bi-rich phase droplet accumulation at the mold side-walls and bottom regions, attaining a maximum number density of $2.0 \times 10^{29} \text{ m}^{-3}$. Figure 7(b) shows the variation in the number density of droplets along the symmetry axis O₁O₂. Under long-time ultrasounds condition, most droplets are concentrated near the point O₁ with a quantity of approximately $2.0 \times 10^{29} \text{ m}^{-3}$, and then decrease sharply to

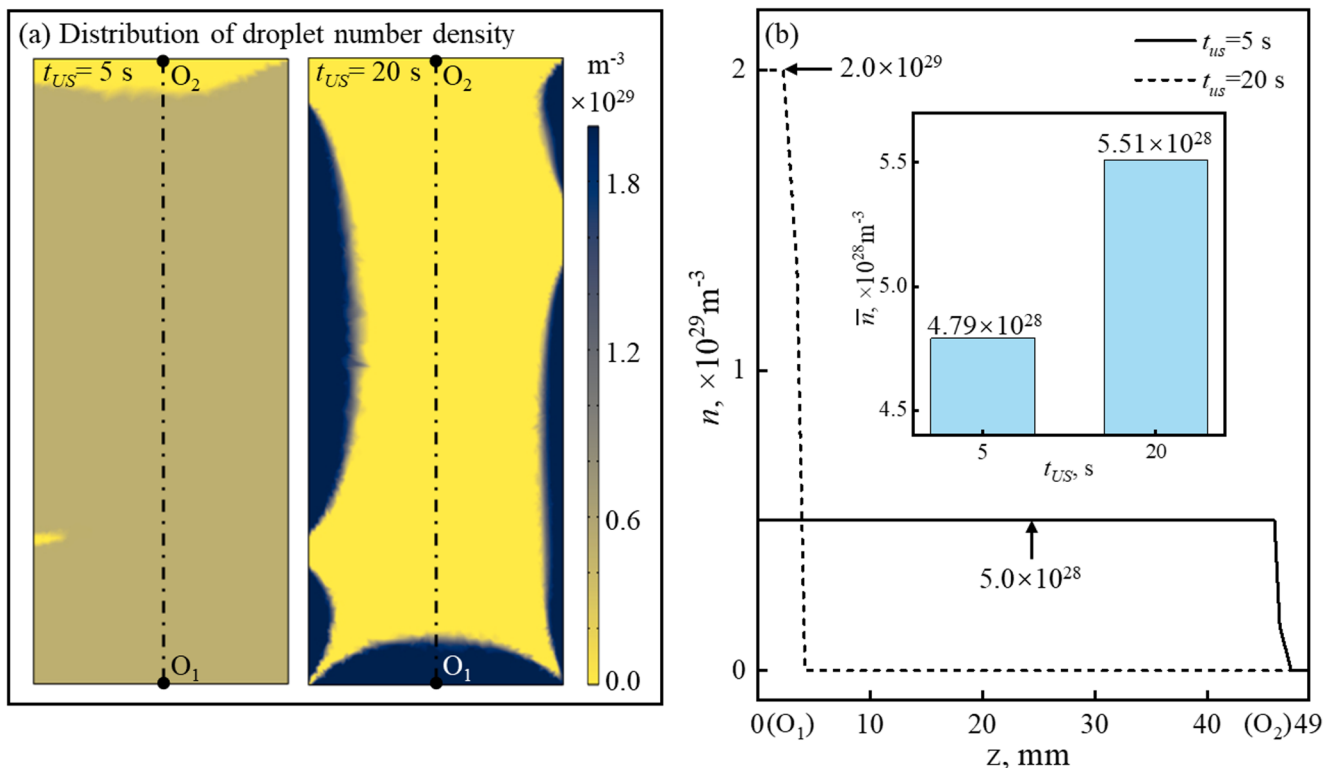


Fig. 7 Number density characteristics of Bi-rich phase droplets under long-time and short-time ultrasounds conditions. (a) the distribution cloud map of droplet number density within the longitudinal section;

(b) the number density variation of Bi-rich phase droplets along the axis O_1O_2 , and the sugfigure presents the averaged droplet number density versus ultrasonic processing time

0 along the height. However, the droplets under short-time ultrasounds condition, maintaining approximately $5.0 \times 10^{28} \text{ m}^{-3}$, are distributed more uniformly along the height, and then decrease to zero only near the point O_2 . As shown in the histogram of Fig. 7(b), the average number density of droplets in the melt under long-time and short-time ultrasounds conditions is approximately $5.51 \times 10^{28} \text{ m}^{-3}$ and $4.79 \times 10^{28} \text{ m}^{-3}$, respectively, which indicates that long-time ultrasounds can promote the nucleation of secondary droplets to some extent. However, long-time ultrasounds promote droplet accumulation in the bottom region of the mold, but the low flow strength is hard to restrain droplet migration, ultimately leading to the formation of Bi-rich phase segregation.

The nucleated droplets gradually coarsen under the Ostwald ripening effect, and subsequently migrate due to the combined effects of surface tension and gravity. When bubbles collapse, the near droplets readily fracture under the high pressure and shockwave. According to the literature [34, 35], the fragmentation of Bi-rich phase droplet requires the shockwave pressure to exceed the Laplace pressure between the two liquid phases $P_L = 2\gamma/R_D$ [36], where γ represents the interfacial tension between the two liquid phases. Wei [37] and Liu [38] suggested that the droplets precipitated during the monotectic reaction typically have radii below 1 μm . Therefore, only Bi-rich droplet with a

radius exceeding 1 μm is considered in the following discussion. Figure 8(a) shows that the peak pressure ($P_{w,max}$) of the shockwave generated during bubble collapse is analyzed for initial radii ranging from 1 μm to 25 μm . The results reveal that $P_{w,max}$ is approximately 2.7 MPa for a 1 μm radius bubble and increases significantly with bubble size, whereas the Laplace pressure of a 1 μm droplet (~ 0.68 MPa) is considerably lower than the instantaneous pressure generated by bubble collapse. This confirms that the shockwave generated during bubble collapse is sufficient to fragment Bi-rich droplet across all radii considered. Furthermore, as shown in Fig. 8(b), the cavitation volume fraction ($f_1 = \text{cavitation region volume}/\text{total melt volume} \times 100\%$) is quantified for bubbles of varying radii under long-time and short-time ultrasounds condition. For a bubble with a radius of 1 μm , the cavitation volume fraction f_1 reaches 5.2% under long-time ultrasounds condition, indicating limited collapse capability at this size. The cavitation volume fraction increases with bubble radius (R_0), reaching 77.7% for a 25 μm bubble. Under short-time ultrasounds condition, f_1 increases from 64.8% at $R_0 = 1 \mu\text{m}$ to 98.1% at $R_0 = 25 \mu\text{m}$. These findings demonstrate that reducing the ultrasound application time minimizes acoustic shielding effects, thereby enhancing the efficiency of droplet fragmentation induced by bubble cavitation. Additionally, when the shear rate of the flow field $\delta > \gamma C_a^*/R_D \cdot \mu_2$,

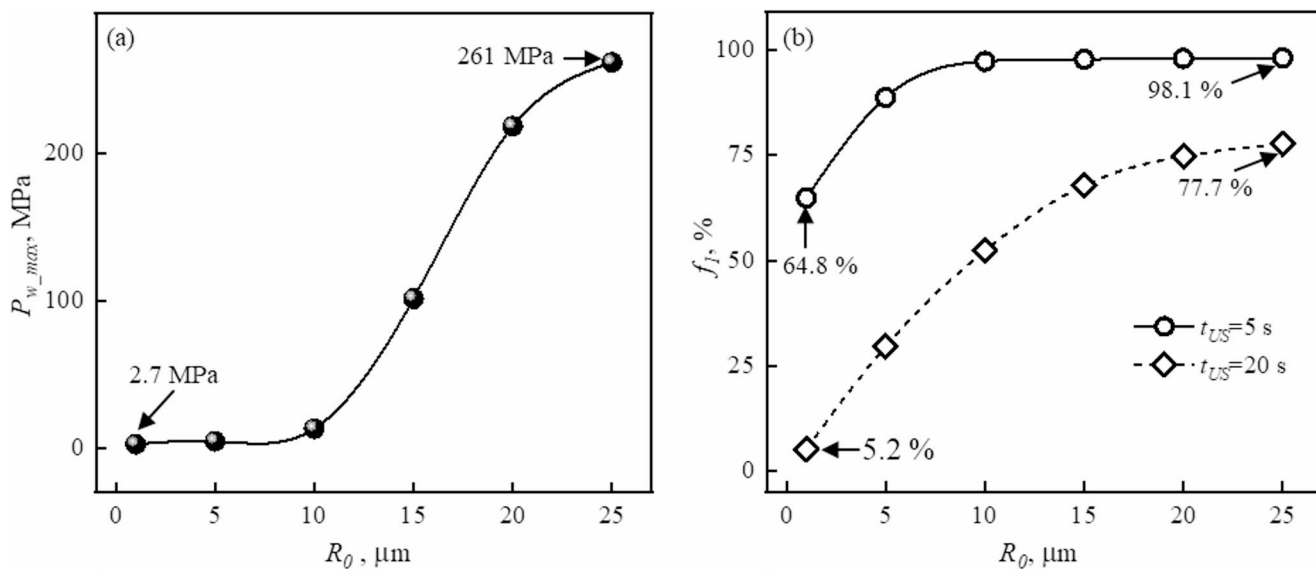


Fig. 8 Calculated bubble cavitation and secondary droplet fragmentation. (a) the peak pressure generated by bubble collapse versus bubble radius; (b) the volume proportion of the melt where the droplet can be fragmented

(H₂O)-rich phase droplets can be stretched, deformed and broken into many finer droplets [31]. For Cu-33%Sn-15%Bi immiscible alloy, the maximum shear rates of the flow field under two different ultrasounds durations are 380 s⁻¹ and 600 s⁻¹, respectively. Calculations reveal that the minimum radii of Bi-rich phase droplets to be fragmented are 3.90 m and 2.46 m, both significantly larger than the droplet sizes formed during the liquid phase separation process. Therefore, it can be concluded that droplet fragmentation in this alloy system is predominantly governed by bubble cavitation rather than acoustic streaming.

3.3.3 Mechanism of acoustic streaming promoting Bi-rich phase droplet migration

During the liquid phase separation process of Cu-33%Sn-15%Bi immiscible alloy, Bi-rich phase droplets are mainly governed by Brownian motion when their radii are less than 1 μm [29, 36, 39]. With the growth of secondary droplet, Stokes migration induced by gravity becomes the dominant effect, which can be described as follows [8, 17]:

$$v_s = \frac{2g(\rho_2 - \rho_1)(\mu_1 + \mu_2)}{3\mu_1(2\mu_1 + 3\mu_2)} R_D^2 \quad (13)$$

where g is the acceleration of gravity and its value is 9.8 m/s². Figure 9(a) gives the relationship between Stokes migration rate v_s and the radius of Bi-rich phase droplet R_D under static condition. As R_D grows from 0 to 200 μm, v_s monotonically increases to 9.89 cm/s. As shown in Fig. 6(b), the global circulation induced by 3D ultrasounds within the melt can hinder the coalescence and sedimentation of

Bi-rich phase droplets and transport droplets throughout the melt. To reveal the influence of flow field under different ultrasound application time on droplet coarsening and coalescence, the volume proportions of effective acoustic streaming f_2 are calculated for both conditions. Here, effective acoustic streaming is defined as that the flow velocity component opposing the gravitational direction should be larger than Stokes migration rate, and the result is illustrated in Fig. 9(b). It can be observed that f_2 decreases with increasing secondary droplet size under the two conditions, whereas this proportion remains consistently lower for long-time ultrasounds condition compared to short-time ultrasounds condition. For instance, when the droplet size is 200 μm, f_2 is approximately 17% under long-time ultrasonic condition and rises to 32.4% under short-time ultrasounds. Therefore, it is more effective to suppress droplet sedimentation by reducing the ultrasounds duration.

In summary, short-time ultrasounds maximize cavitation effect (enabling droplet fragmentation via high sound pressure) and acoustic streaming effect (promoting uniform distribution via strong flow), effectively countering sedimentation. Conversely, long-time ultrasounds significantly increase bubble content, which attenuates sound energy, weakens cavitation and flow, and reduces the efficiency of droplet fragmentation and migration, thereby leading to the occurrence of macroscopic segregation.

3.4 Liquid phase separation mechanism under different ultrasound application time

Based on the above works, we systematically elucidate the temporal effects of ultrasound irradiation on liquid phase

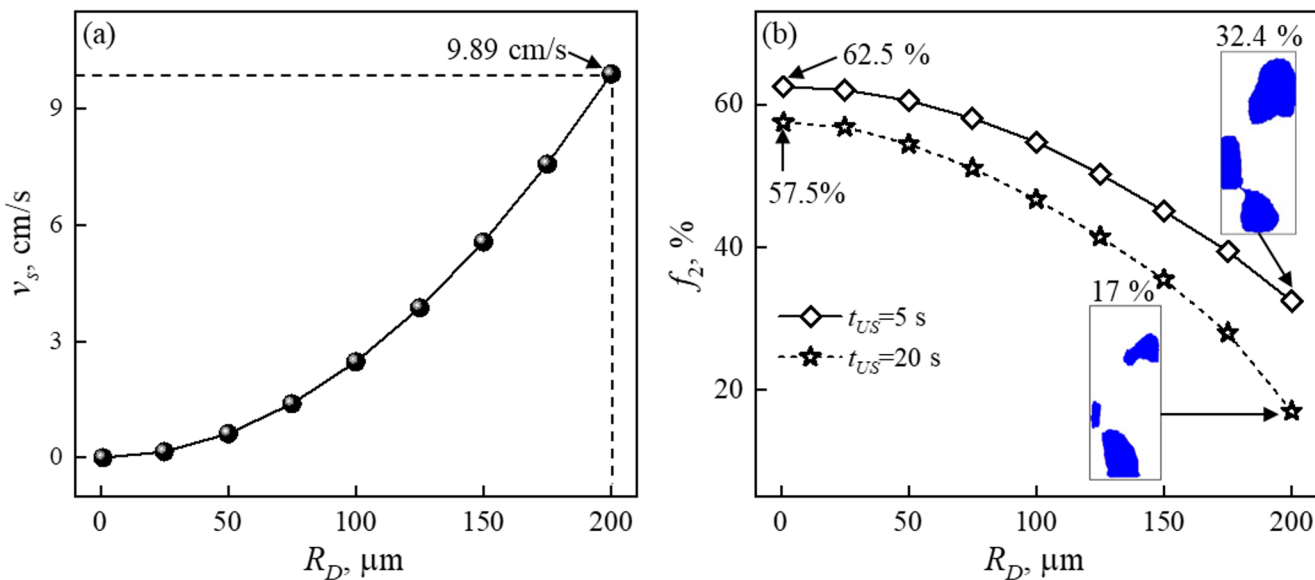


Fig. 9 Calculated bubble cavitation and secondary droplet fragmentation. (a) the peak pressure generated by bubble collapse versus bubble radius; (b) the volume proportion of the melt where the droplet can be fragmented

separation evolution in ternary Cu-33%Sn-15%Bi immiscible alloy, as shown in Fig. 10. During the static solidification process, the phase separation initiates when the melt enters the immiscibility gap. The secondary droplets experience coarsening and sedimentation, ultimately gathering at the alloy melt bottom dominated by Marangoni and Stokes forces, as shown in Figs. 10(a₁)-(a₃). Subsequently, the primary Cu₃Sn phase nucleates, grows, and finally forms a severely layered solidified structure, as described in Fig. 10(a₄). When 3D ultrasounds are imported into the liquid phase separation process, the dissolved gas in the melt is excited to nucleate and grow into gas bubbles. When short-time ultrasounds are applied in the final stage of liquid phase separation, the cavitation region generally occupies most of the area except the melt top, where the bubbles occur violent collapse, accompanied by the formation of local high undercooling and microjets, which greatly promotes the secondary droplet nucleation, as seen in Figs. 10(b₁) and (b₂). Meanwhile, the flow strength of the global circulation is strong enough to drive these droplets to offset the Stokes sedimentation and migrate throughout the whole melt. After the end of liquid phase separation, the primary Cu₃Sn phase begins to nucleate and consequently traps the bubbles that fail to escape from the melt in time. As a result, the solidified microstructure exhibits many pores across its surface, as seen in Figs. 10(b₃) and (b₄). Under the long-time ultrasounds condition, the cavitation region is shrunk and only forms near the sidewalls and bottom of the mold, which attenuates droplet nucleation and fragmentation (Fig. 10(c₁)). However, the increase in ultrasounds duration enhances the acoustic shielding effect and subsequently reduces the acoustic streaming magnitude. The low

flow strength makes it difficult to suppress Stokes migration of the droplet, resulting in Bi-rich phase accumulation at the melt bottom. Furthermore, the number of gas bubbles exhibits a positive correlation with the ultrasounds durations, thus the amount of gas bubbles trapped in the solid Cu₃Sn phase increases with the extension of ultrasound application time, as described in Figs. 10(c₃) and (c₄). Therefore, the application of short-time ultrasounds at the final stage of liquid phase separation is more conducive to preparing a solidification structure with uniformly distributed Bi particles on Cu₃Sn matrix and resulting in a significant reduction in porosity.

3.5 Corrosion and tribological properties after ultrasonic solidification

3.5.1 Electrochemical corrosion resistance

Figure 11 presents the potentiodynamic polarization curves and impedance spectra in 3.5% NaCl solution at room temperature for Cu-33%Sn-15%Bi immiscible alloy. In Figs. 11(a) and (b), the self-corrosion potential (E_{corr}) of all samples is negative, indicating that this alloy has a high corrosion sensitivity. Under static condition, the self-corrosion potential and current density are approximately -1.25 V and 36.57 $\mu\text{A}/\text{cm}^2$, respectively. When 3D ultrasounds are introduced during the liquid-phase separation process, the alloy samples exhibit a significant increase in self-corrosion potential and a decrease in corrosion current density. Especially for the sample treated by short-time ultrasounds, it exhibits good corrosion resistance with the highest self-corrosion potential and the lowest self-corrosion current

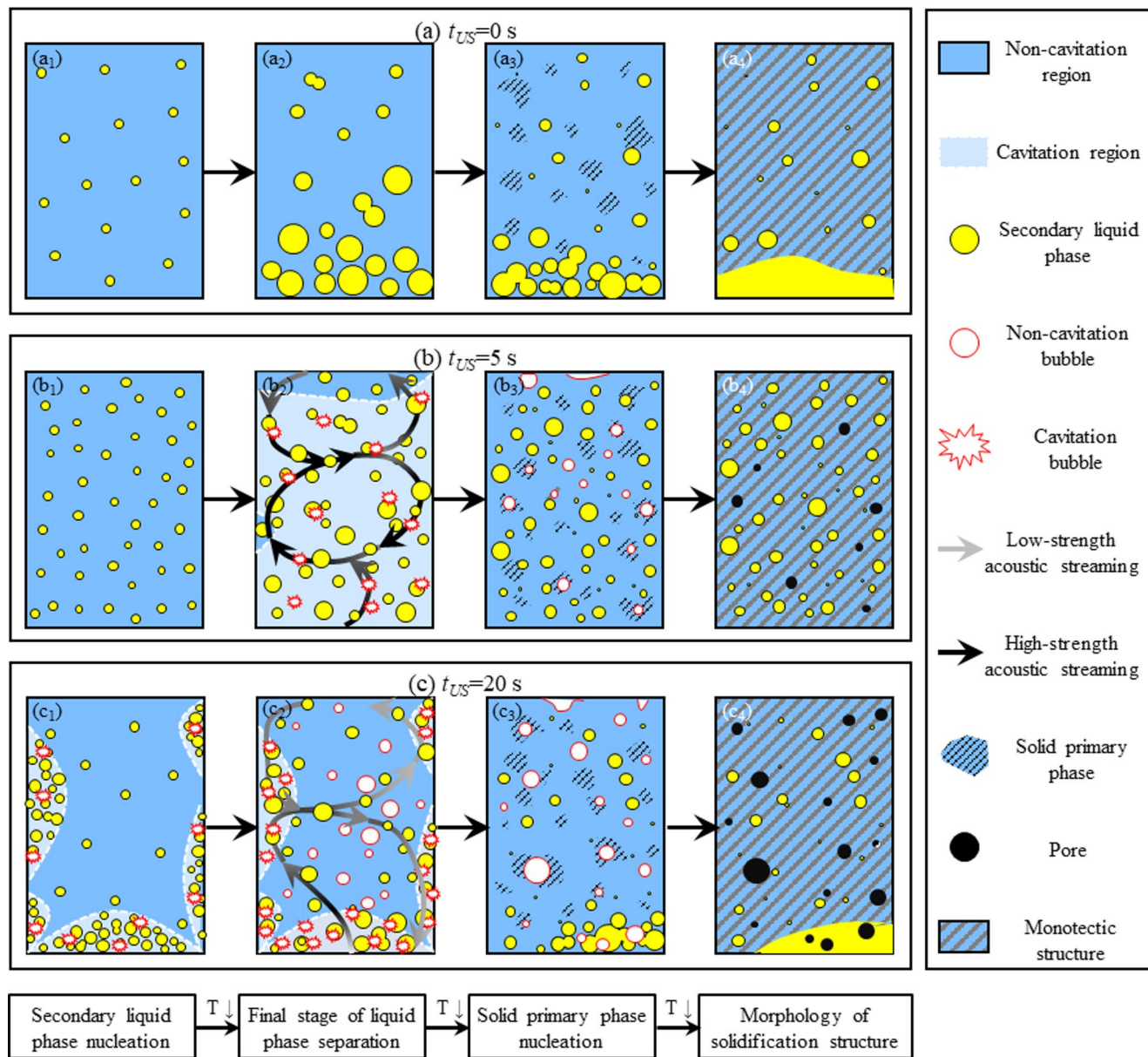


Fig. 10 Illustration of liquid phase separation mechanism of Cu-33%Sn-15%Bi alloy within ultrasonic field. **(a)** $t_{US}=0\text{ s}$; **(b)** $t_{US}=5\text{ s}$; **(c)** $t_{US}=20\text{ s}$

density of -1.02 V and $5.34\text{ }\mu\text{A}/\text{cm}^2$, respectively. The electrochemical impedance spectroscopy measurements are illustrated in Figs. 11(c) and (d). Compared to static condition, samples processed under short-time ultrasounds condition exhibit the highest impedance film value ($|z|$) and single-phase angle (θ), which means that this solidification condition greatly improves the corrosion resistance of the alloy and results in a more uniform corrosion distribution on the surface. Liu [8], Wang [40], and Osório [41] suggest that the corrosion resistance of Cu_3Sn intermetallic compound is significantly better than that of Bi-rich phase. The homogeneous dispersion of the microstructure reinforces the continuity of Cu_3Sn matrix, while the fine and uniform

distribution of Bi-rich particles mitigates localized corrosion cells, collectively facilitating the formation of a more stable and superior protective film. Meanwhile, the refined microstructure significantly increases grain boundary density, which enhances polarization resistance and acts as an effective barrier against the penetration of corrosive species.

3.5.2 Tribological property

The friction and wear properties of alloy samples under different solidification conditions are presented in Fig. 12, in which Figs. 12(a) and (b) illustrate the time-dependent variation of the friction coefficient for the top and

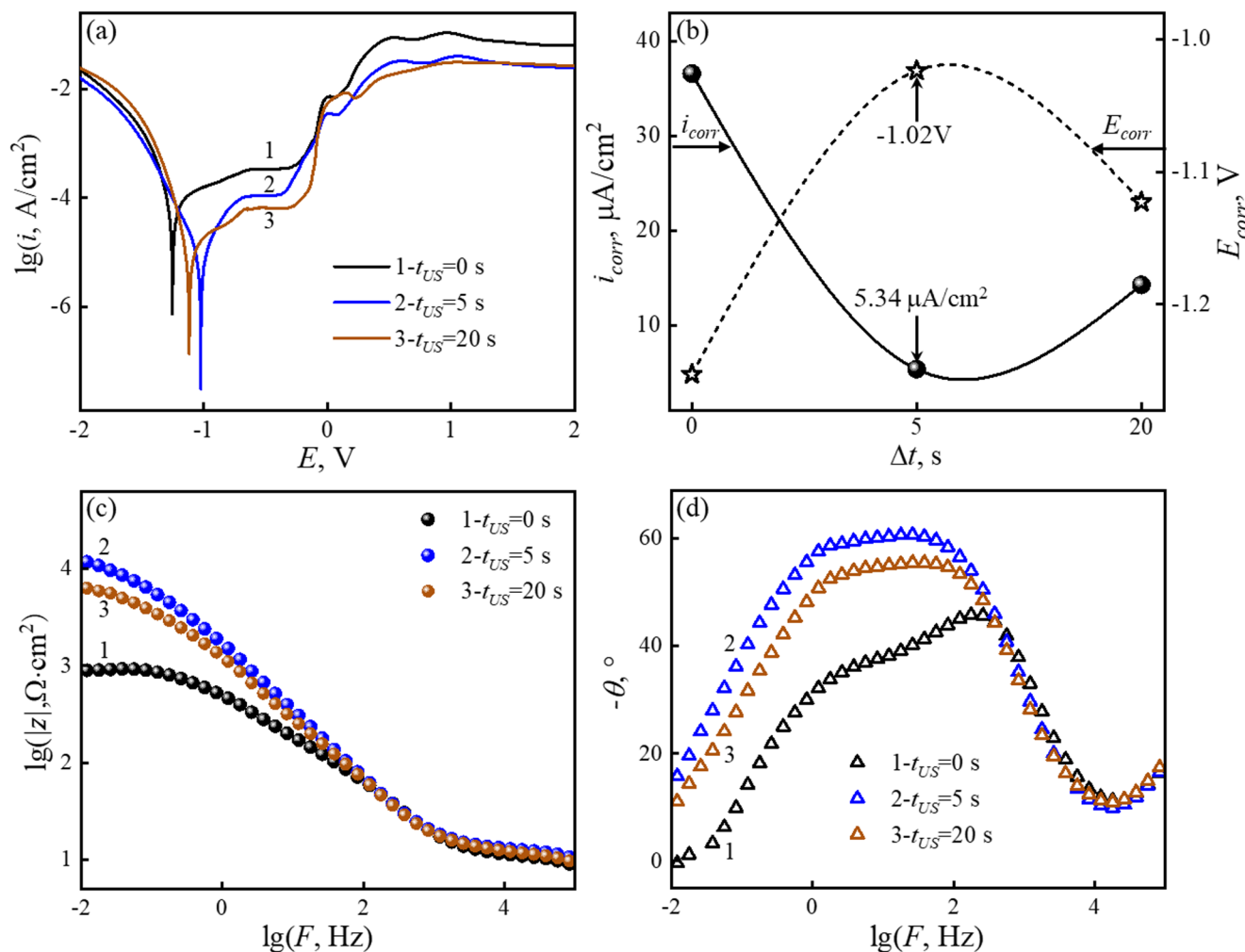


Fig. 11 Electrochemical corrosion resistance of Cu-33%Sn-15%Bi alloy in 3.5% NaCl solution. (a) polarization curves; (b) the change of self-corrosion potential and current density; (c) impedance film value; (d) single-phase angle

bottom regions of the samples, respectively. The top region exhibits minimal variation in the friction coefficient across all conditions, while the bottom region demonstrates a significantly lower coefficient under short-time ultrasounds condition and a nearly steady variation pattern over time. In contrast, other conditions reveal severe inhomogeneity due to the presence of the Bi-rich phase segregation layer at the bottom. This is because the soft (Bi) phase with a low melting point tends to fall off from the surface during friction, thereby increasing the contact area with the anti-grinding material. Figures 12(c) and (d) display the 3D profilometry images of the wear track under static and short-time ultrasounds conditions, respectively. The bottom of the static sample shows a severe wear loss and its maximum wear depth reaches $53.46 \mu\text{m}$. However, both wear depth and pit size are significantly improved by short-time ultrasounds, which is primarily attributed to a dual mechanism combining dispersion strengthening and in-situ self-lubrication. The uniformly distributed hard Cu_3Sn matrix forms a

continuous framework that effectively resists abrasive wear, while the finely dispersed Bi-rich particles, characterized by a low melting point, exude under frictional heating to form a continuous lubricating film. This film not only reduces frictional heat and surface temperature but also minimizes direct abrasive contact, thereby substantially reducing wear volume and surface damage.

4 Conclusions

The effect of 3D ultrasounds on the microstructure and physical properties of ternary Cu-33%Sn-15%Bi immiscible alloy are systematically investigated by combining experimental analysis and numerical simulations. The main conclusions are as follows:

- (1) Compared to the limited segregation suppression under long-time 3D ultrasounds, applying short-time 3D

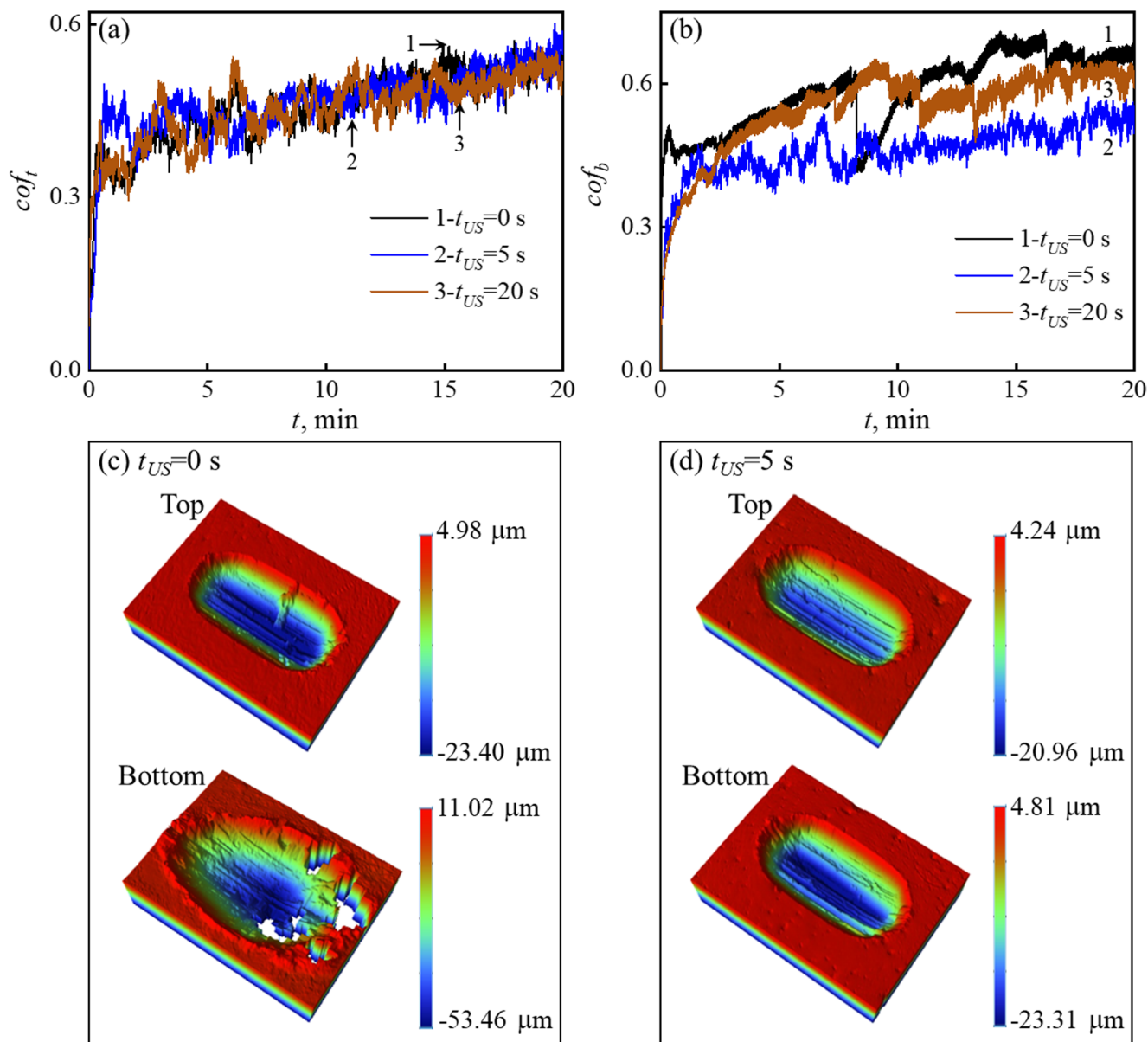


Fig. 12 Friction and wear properties. (a) friction coefficient at the top region; (b) friction coefficient at the bottom region; (c) wear track at $t_{US}=0$ s; (d) wear track at $t_{US}=5$ s

ultrasounds during the final stage of liquid-phase separation significantly eliminates the macro/micro segregation and refines Bi-rich phase droplets.

- (2) Although short-time ultrasounds reduce the nucleation rate of Bi-rich phase droplets facilitated by cavitation, it effectively weakens the acoustic shielding effect by decreasing the gas bubble content in alloy melt. This significantly enlarges the volume fraction of the cavitation region and enhances the effective acoustic streaming, thereby improving droplet fragmentation and inhibiting Stokes migration.
- (3) The electrochemical corrosion resistance of the alloy is significantly enhanced by short-time 3D ultrasounds,

primarily attributed to the refinement and homogenized distribution of Bi-rich phase droplets on the hard Cu3Sn matrix. This also facilitates the formation of a continuous and coherent lubricating film during friction processes, leading to a remarkable improvement in alloy's tribological performance.

Acknowledgements This work was financially supported by National Natural Science Foundation of China (Nos. 52130405, 52088101, U24A20206), and Research Plan of Shaanxi Province (No: 2023-JC-JQ-28, 2025SYS-SYSZD-095).

Author contributions Ying Zhang Data curation; Investigation; Methodology; Software; Writing-original draft. Wenhua Wu Investigation; Validation, Supervision; Writing-review & editing. Jianyuan Wang

Funding acquisition; Investigation; Supervision; Validation; Writing-review & editing. Wei Zhai Funding acquisition; Methodology; Supervision; Writing-review & editing.

Data availability The data that support the fundings of this study are available on request from the corresponding author upon reasonable request.

Declarations

Competing interests All authors certify that they have no affiliations with or involvement in any organization or entity with any financial interest or non-financial interest in the subject matter or materials discussed in this manuscript.

References

- I. Kaban, M. Köhler, L. Ratke, J. Eckert, A.L. Greer et al., Interfacial tension, wetting and nucleation in Al-Bi and Al-Pb monotectic alloys. *Acta Mater.* **59**(18), 6880–6889 (2011). <https://doi.org/10.1016/j.actamat.2011.07.031>
- W.L. Wang, Z.Q. Li, B. Wei, Macrosegregation pattern and microstructure feature of ternary Fe-Sn-Si immiscible alloy solidified under free fall condition. *Acta Mater.* **59**(14), 5482–5493 (2011). <https://doi.org/10.1016/j.actamat.2011.05.022>
- Y.C. Wang, L.X. Zhang, J. Luo et al., Evaluation of the segregation in printed mono-sized Al-In alloy droplets. *J. Mater. Process Technol.* **326**, 118339 (2024). <https://doi.org/10.1016/j.jmatprotec.2024.118339>
- R.P. Shi, C.P. Wang, D. Wheeler et al., Formation mechanisms of self-organized core/shell and core/shell/corona microstructures in liquid droplets of immiscible alloys. *Acta Mater.* **61**(4), 1229–1243 (2013). <https://doi.org/10.1016/j.actamat.2012.10.033>
- Q. Sun, H.X. Jiang, J.Z. Zhao et al., Microstructure evolution during the liquid-liquid phase transformation of Al-Bi alloys under the effect of tic particles. *Acta Mater.* **129**, 321–330 (2017). <https://doi.org/10.1016/j.actamat.2017.02.071>
- H. Chen, J.L. Bai, Y. Liu et al., An improved Preparation method of core-shell Al@Sn-Bi microspheres and its microstructure formation mechanism. *J. Mater. Process Technol.* **328**, 118415 (2024). <https://doi.org/10.1016/j.jmatprotec.2024.118415>
- S.Z. Zhao, S.F. Zhou, M. Xie et al., Phase separation and enhanced wear resistance of Cu88Fe12 immiscible coating prepared by laser cladding. *J. Mater. Res. Technol.* **8**(2), 2001–2010 (2019). <https://doi.org/10.1016/j.jmrt.2018.12.018>
- J.M. Liu, W.H. Wu, W. Zhai et al., Ultrasonic modulation of phase separation and corrosion resistance for ternary Cu-Sn-Bi immiscible alloy. *Ultrason. Sonochem.* **54**, 281–289 (2019). <https://doi.org/10.1016/j.ultrsonch.2019.01.029>
- S.V. Komarov, T. Yamamoto, J.C. Sun, Fabrication of Al-Bi frozen emulsion alloys due to high-intense ultrasound irradiation. *J. Alloy Compds.* **859**, 158231 (2021). <https://doi.org/10.1016/j.jallcom.2020.158231>
- Y.Q. Li, H.X. Jiang, H. Sun et al., Microstructure evolution of immiscible alloy solidified under the effect of composite electric and magnetic fields. *J. Mater. Sci. Technol.* **162**, 247–259 (2023). <https://doi.org/10.1016/j.jmst.2023.04.018>
- I.G. Eskin, D.G. Eskin, Ultrasonic treatment of light alloy melts. (CRC Press, 2014)
- H.R. Kotadia, A. Das, E. Doernberg et al., A comparative study of ternary Al-Sn-Cu immiscible alloys prepared by conventional casting and casting under high-intensity ultrasonic irradiation. *Mater. Chem. Phys.* **131**(1–2), 241–249 (2011). <https://doi.org/10.1016/j.matchemphys.2011.09.020>
- W.H. Wu, J.Y. Wang, W. Zhai et al., A computational and experimental study of ultrasonicated phase separation process for liquid Al-Bi immiscible alloy. *Metall. Mater. Trans. B* **54**, 1845–1857 (2023). <https://doi.org/10.1007/s11663023-02799-0>
- Y. Pan, D.L. Lu, Y.Q. Li et al., Origin of the antioxidation mechanism of RuAl(1 1 0) surface from first principles calculations. *Mat. Sci. Eng. B* **259**, 114580 (2020). <https://doi.org/10.1016/j.mseb.2020.11458>
- Y. Pan, Ab-initio calculations of mechanical and thermodynamic properties of TM (transition metal: 3d and 4d)-doped Pt₃Al. *Vacuum.* **156**, 419–426 (2018). <https://doi.org/10.1016/j.vacuum.2018.08.010>
- H.J. Huang, L. Qin, H.B. Tang et al., Ultrasound cavitation induced nucleation in metal solidification: an analytical model and validation by real-time experiments. *Ultrason. Sonochem.* **80**, 105832 (2021). <https://doi.org/10.1016/j.ultrsonch.2021.105832>
- W.H. Wu, D.Z. Wang, W. Zhai et al., Multiple ultrasounds assisted phase separation and monotectic solidification of liquid ternary Al_{81.5}Cu_{14.7}Bi_{3.8} immiscible alloy. *J. Appl. Phys.* **133**, 115102 (2023). <https://doi.org/10.1063/5.0135344>
- D.G. Eskin, I. Tzanakis, F. Wang et al., Fundamental studies of ultrasonic melt processing. *Ultrason. Sonochem.* **52**, 455–467 (2019). <https://doi.org/10.1016/j.ultrsonch.2018.12.028>
- W.W. Xu, I. Tzanakis, P. Srirangam, A.J. Bodey, P.D. Lee et al., Synchrotron quantification of ultrasound cavitation and bubble dynamics in Al-10Cu melts. *Ultrason. Sonochem.* **31**, 355–361 (2016). <https://doi.org/10.1016/j.ultrsonch.2016.01.017>
- O. Behrend, H. Schubert, Influence of hydrostatic pressure and gas content on continuous ultrasound emulsification. *Ultrason. Sonochem.* **8**(3), 271–276 (2001). [https://doi.org/10.1016/S1350-4177\(01\)00088-8](https://doi.org/10.1016/S1350-4177(01)00088-8)
- G.N. Sahadeva, A.S. Ravindran, T. Chandrashaker et al., Influence of ultrasonic vibrations on grain size and mechanical properties of A-356 by adding Al-5Ti-1B master alloy during solidification. *Int. J. Sci. Res.* **5**, (2015).
- R. Venkatesh, K. Logesh, S. Singh et al., Aluminium alloy nanocomposite made with SiC via ultrasonic stir casting: behaviour study. *J. Mech. Sci. Technol.* **38** (2024). <https://doi.org/10.1007/s12206-024-0711-y>
- A. Korgal, S. Upadhyaya, T. Anilkumar et al., Grain refinement of aluminium 4032 alloy with the impact of vibration using Taguchi technique and analysis of variance (ANOVA). *Mater. Today.* **54**, 507–512 (2022). <https://doi.org/10.1016/j.matpr.2021.11.504>
- Y.J. Hu, J.Y. Wang, N.X. Xu et al., Three orthogonally arranged ultrasounds modulate solidification microstructures and mechanical properties for AZ91 magnesium alloy. *Acta Mater.* **241**, 118382 (2022). <https://doi.org/10.1016/j.actamat.2022.118382>
- X.S. Chen, Q.B. Bayanheshig, Jiao et al., Numerical simulation of ultrasonic enhancement by acoustic streaming and thermal effect on mass transfer through a new computation model. *Int. J. Heat. Mass. Transf.* **171**, 121074 (2021). <https://doi.org/10.1016/j.ijheatmasstransfer.2021.121074>
- S. Min, J. Park, J. Lee, Surface tension of the 60%Bi–24%Cu–16%Sn alloy and the critical temperature of the immiscible liquid phase separation. *Mater. Lett.* **62**(29), 4464–4466 (2008). <https://doi.org/10.1016/j.matlet.2008.08.007>
- J. Lighthill, Acoustic streaming. *J. Sound Vib.* **61**(3), 391–418 (1978). [https://doi.org/10.1016/0022460X\(78\)90](https://doi.org/10.1016/0022460X(78)90)
- S. Tjøtta, Theoretical investigation of heat and streaming generated by high intensity ultrasound. *Acta Acust United Acust* **85**, 780–787 (1999)

29. T. Trummler, S.J. Schmidt, N.A. Ndams, Numerical investigation of non-condensable gas effect on vapor bubble collapse. *Phys. Fluids* **33**(9), 096107 (2021). <https://doi.org/10.1063/5.0062399>
30. A.V. Pandit, V.P. Sarvothaman, V.V. Ranade, Estimation of chemical and physical effects of cavitation by analysis of cavitating single bubble dynamics. *Ultrason. Sonochem.* **77**, 105677 (2021). <https://doi.org/10.1016/j.ultsonch.2021105677>
31. B.Q. Ma, J.Q. Li, Z.J. Peng et al., Structural morphologies of Cu-Sn-Bi immiscible alloys with varied compositions. *J. Alloy Compds.* **535**, 95–101 (2012). <https://doi.org/10.1016/j.jallcom.2012.04.032>
32. J. Valloton, S. Gawor, H. Henein, Modelling of nucleation in impulse atomized undercooled droplets. *Comput. Mater. Sci.* **144**, 176–180 (2018). <https://doi.org/10.1016/j.commatsci.2017.12.004>
33. B. Arfaei, M. Benedict, E.J. cotts, Nucleation rates of Sn in undercooled Sn-Ag-Cu flip-chip solder joints. *J. Appl. Phys.* **114**, 173506 (2013). <https://doi.org/10.1063/1.4826437>
34. Z. Ying, W.H. Wu, J.Y. Wang et al., In-situ observation of phase separation dynamics for immiscible aqueous solution within ultrasonic field. *Ultrason. Sonochem.* **100**, 106634 (2023). <https://doi.org/10.1016/j.ultsonch.2023.106634>
35. W.H. Wu, D.G. Eskin, A. Priyadarshi et al., New insights into the mechanisms of ultrasonic emulsification in the oil-water system and the role of gas bubbles. *Ultrason. Sonochem.* **73**, 105501 (2021). <https://doi.org/10.1016/j.ultsonch.2021.105501>
36. K. Doi, H. Ohtani, M. Hasebe, Thermodynamic study of the phase equilibria in the Sn-Ag-Bi-Cu quaternary system. *Mater. Trans.* **45**(2), 380–383 (2004). <https://doi.org/10.2320/matertrans.45.380>
37. C. Wei, J. Wang, Y.X. He et al., Influence of high magnetic field on the liquid-liquid phase separation behavior of an undercooled Cu-Co immiscible alloy. *J. Alloy Compds.* **842**, 155502 (2020). <https://doi.org/10.1016/j.jallcom.2020.155502>
38. S.C. Liu, J.C. Jie, B.W. Dong et al., Novel insight into evolution mechanism of second liquid-liquid phase separation in metastable immiscible Cu-Fe alloy. *Mater. Des.* **156**, 71–81 (2018). <https://doi.org/10.1016/j.matdes.2018.06.044>
39. H. Tanaka, A new coarsening mechanism of droplet spinodal decomposition. *J. Chem. Phys.* **103**, 2361–2364 (1995). <https://doi.org/10.1063/1.469658>
40. X. Wang, M.Y. Nie, C.T. Wang et al., Microhardness and corrosion properties of hypoeutectic Al-7Si alloy processed by high-pressure torsion. *Mater. Des.* **83**, 193–202 (2015). <https://doi.org/10.1016/j.matdes.2015.06.018>
41. W.R. Osório, E.S. Freitas, A. Garcia, EIS and potentiodynamic polarization studies on immiscible monotectic Al-In alloys. *Electrochim. Acta* **102**, 436–445 (2013). <https://doi.org/10.1016/j.electacta.2013.04.047>

Publisher's note Springer Nature remains neutral with regard to jurisdictional claims in published maps and institutional affiliations.

Springer Nature or its licensor (e.g. a society or other partner) holds exclusive rights to this article under a publishing agreement with the author(s) or other rightsholder(s); author self-archiving of the accepted manuscript version of this article is solely governed by the terms of such publishing agreement and applicable law.